

Velocity Distribution of Fragments Formed in a Simulated Collisional Disruption

AKIKO NAKAMURA AND AKIRA FUJIWARA

Department of Physics, Kyoto University, Kyoto 606 Japan

Received August 15, 1990; revised February 19, 1991

The velocity *distribution* of fragments resulting from catastrophic disruption was determined experimentally which is of great importance to understand the collisional evolution of planetary bodies. Basalt and alumina spheres 6 cm in diameter were shattered by nylon spheres 7 mm in diameter at velocities of 3 ~ 4 km/sec. From high-speed photographic records taken from two orthogonal directions, velocity, initial position, and size of a few hundreds of fragments were obtained using an image processor. The three-dimensional fragment velocity determined for some prominent fragments is expressed as the $-\frac{1}{3}$ power of fragment mass for fragment sizes larger than a few millimeters. The fraction of energy, momentum, and angular momentum partitioned into the large major fragments, core, and the fast fine ejecta from near the impact site were evaluated. About 1% of the initial kinetic energy was found to be partitioned into the major, large fragments. Cores were minor carriers of energy and momentum, while fine ejecta played a significant role as carriers of the three kinetic quantities. © 1991 Academic Press, Inc.

1. INTRODUCTION

The catastrophic disruption of planetary bodies by high-velocity collisions plays a crucial role in the collisional evolution of planetary and asteroidal systems. In the past decade, both experimental and theoretical approaches have been attempted to understand the outcomes of catastrophic disruption. Laboratory studies disrupting small solid targets by hypervelocity projectiles is an effective method as the phenomena are extremely complicated. Laboratory experiments have revealed many different aspects of the catastrophic disruption, for example, fragmentation modes, size distributions, and fragment shapes, for various target materials and impact velocities ranging from tens to thousands of meters per second (e.g., Fujiwara *et al.* 1989, and references therein).

However, measurements of the kinetic aspects of collisional disruption, that is, the velocity and rotational frequency of the individual fragments are rare, and, moreover, their distributions are left almost uninvestigated.

Only selected fragments observed in the pictures obtained by high-speed cameras were tracked and their velocities or rotational frequencies were evaluated (Fujiwara and Tsukamoto 1980, 1981, Takagi and Mizutani 1984, Fujiwara 1987, Davis and Ryan 1990). These reports pointed out the following results:

- (1) The antipodal or mean three dimensional (3-D) velocity of the fragments is scaled in terms of collisional specific energy or nondimensional impact stress, and is typically on the order of 1–10 m/sec when impacted with a specific energy of about 10^7 ergs/g.
- (2) Fragments seem to eject radially from the hypothetical radiant located just beneath the impact point. Fragment velocities are highest near the impact point and decrease with increasing distance from that point for the fragments from the target surface.
- (3) In oblique impacts into spheres, the motion of the fragments is almost symmetrical about the surface normal to the impact point.
- (4) The rotational kinetic energy of individual fragments is at least two orders of magnitude smaller than their translational energy.

A semiempirical model of velocity fields (Paolicchi *et al.* 1989) in which fragments were thought to be “irradiated” from “radiant points” (Fujiwara and Tsukamoto 1980) was constructed to describe the experimental results.

The present work intends to reveal experimentally the velocity *distribution*, which is of great importance for at least two reasons. First, it determines the fraction of impact ejecta that would escape the gravity fields of planetary bodies, which controls the growth of planets by accretion. However, before these results can be applied, scaling laws must be established which allow extrapolation of the results to the regimes appropriate to large-scale collisions. Second, it is used to determine the energy and momentum partitioning in collisional disruption.

In Section 2, the experimental procedure is presented. The analytical procedure to obtain the mass, velocity, and

TABLE I
Experiment Conditions

Target type ^a	Target mass; M_t (g)	Velocity ($\times 10^3$) (cm/sec)	E^b/M_t ($\times 10^7$) (ergs/g)	Core mass fraction	M_{rec} (≥ 5 mg) (g)	M_{rec} (≥ 0 mg) (g)	Number of fragments measured (top, side)	Incident angle to the target surface (deg)
a	395.7	4.00	4.29	0.2481	390.099	392.925	373, 291	60
a2	390.7	4.40	5.28	0.2799	382.015	388.151	(no film)	60
a2*	401.7	3.85	3.93	0.2414	395.883	400.645	(no film)	60
b	303.2	3.2	3.6	0.3115	290.931	300.148	208, 311	60
b*	297.9	3.33	3.91	0.2773	288.378	297.257	(no film)	60
b2	307.0	3.16	3.45	0.2871	298.713	304.454	(no film)	60

^a a, a2, a2*: alumina; b, b*, b2: basalt.

^b Projectile kinetic energy.

initial position of the fragments are outlined in Section 3. Velocity distributions as a function of mass and initial position are presented in Section 4. Energy, momentum, and angular momentum balances are discussed in Section 5. The conclusions are summarized in Section 6.

2. EXPERIMENTS

Impact disruption of one basalt and one alumina sphere was accomplished with a two-stage light-gas gun at Kyoto University while taking pictures. The basalt, supplied from Yakuno, Kyoto, had a density of 2.7 g/cm³. The alumina ceramic spheres were commercially sold and had a density of 3.6 g/cm³ and a nominal compressive strength of 2×10^{10} ergs/cm³. The diameter and mass M_t of the targets are shown in Table I. Basalt and alumina were selected to illustrate any differences in the collisional outcomes that might occur due to differences in material strength and density.

Targets were suspended by threads in a box ($35 \times 50 \times 30$ cm³) made of vinyl chloride. This box, which has acrylic resin windows and an entrance hole of diameter 15 mm for the projectile, was put in the experimental chamber along the trajectory of the gun muzzle. The ambient pressure in the chamber was less than 3.0 Torr. The incident angle was 60° to the surface of the target. The projectiles were nylon spheres 7.0 mm in diameter and mass 0.213 g. Their velocities were 3.2 km/sec and 4.0 km/sec for the basalt and alumina target, respectively.

Two high-speed framing cameras were oriented to view the collisional breakup through the side and top windows of the box. They were fixed at a distance of 250 cm from the targets. The field of view of each camera was about 15×15 cm². The focal distances of the lenses mounted on the cameras were 10 cm, which is sufficient to avoid

errors due to perspective as described later. Targets were illuminated by flash guns through the front and rear windows of the box. To get a good contrast of the objects against the background, a black background was selected for the white alumina target and a green one for the gray basalt target. The framing rate of the camera was fixed to be 6000 frames/sec.

One more basalt sphere was shattered under the same conditions but we missed taking films. Fragments with enough kinetic energy would break again when they hit the interior surface of the box. To get a mass distribution without serious secondary fragmentation effects we shot another basalt and two alumina targets in the box whose interior was lined with styrofoam board 1.8 cm thick and doubly layered 1 cm thick urethane sheets. The shot conditions were the same as before; however, no pictures were taken.

3. ANALYSIS

After the films were dubbed, frame by frame, onto videotape, they were analyzed using an image processor. The frame is divided as a 512×512 grid (i.e., 262,144 picture elements), whose brightness is discriminated in 0–255 grades. First, we made the picture a bicolor one to discriminate individual fragments from the background. If the picture was an ideal one where the fragments and the background are clearly distinctive, we could process it automatically using a standard image processing program with a suitable value adopted for the brightness threshold. However, in practice, it was difficult to process a picture with only one brightness threshold for the whole region of a frame, because there was no uniformity in the brightness even in the background, owing mainly to the shadows made by fragments. Moreover, many of the images of the

fragments overlapped each other. Therefore, the outlines of the fragments were drawn manually first, then the frame was processed into a bicolor picture part by part referring to the images in the successive frames to distinguish fragments from noises and stains on the window.

On each frame, positions and sizes of the fragments were measured, where position was defined by the center of gravity of the fragment image, and the size was defined by the average of the vertical and horizontal widths of the fragment image. They were calibrated by referring to the initial position and size of the targets. Each picture element corresponded to a 0.034×0.034 -cm square in the field of view, i.e., the resolution was 0.034 cm. The camera-to-fragment distances were different for each individual fragment, but were within 250 ± 10 cm. The object-to-image (on the films) size ratio was approximately 10 cm/(250 ± 10) cm. Therefore, errors in measurement of positions and sizes of the fragments on the films due to perspective were not more than 4% and were neglected. Dominant errors arose both from the effect of rotations of the individual fragments and from the incomplete outlining of the images, which finally result in the sigmas shown in Figs. 6a and 6b below.

Recovered fragments were weighed by an electronic balance down to 5 mg and the original target spheres were reconstructed as far as possible to be compared with images of the fragments on the films.

Table I shows the initial conditions and the outcomes for the basalt (b, b*) and alumina (a) shots and also those for the shots into a basalt sphere (b2) and alumina (a2, a2*) spheres surrounded by soft materials which were used to avoid secondary destruction. Some sample top-view frames are shown in Figs. 1a and 1b. Figure 1c illustrates the geometrical configuration of the top and side views. Scores of frames were sampled for the analysis from frames during 10 ~ 15 msec postcollision. Hundreds of fragment images (those larger than four picture elements) were tracked on the films. The total number of fragments on the films identified with the recovered ones (some of the correspondence was one fragment image to several recovered ones as mentioned in the next section) were 60 for alumina (a) and 39 for basalt (b) experiments.

4. RESULTS

Mass Distribution of the Fragments

In each of the six shots, the largest fragment was left intact at the center of the original target sphere (called the

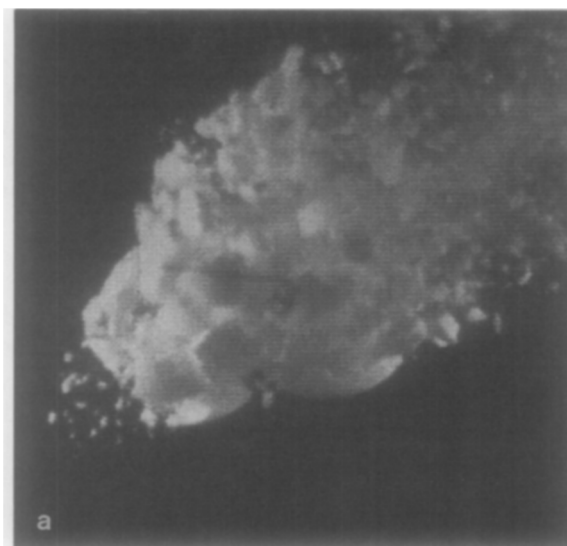
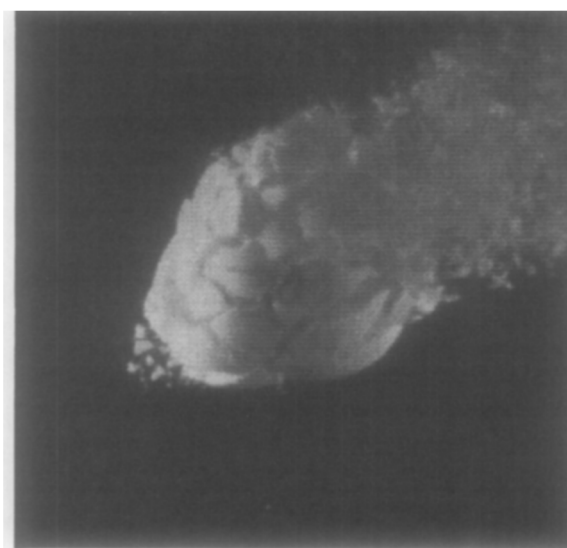
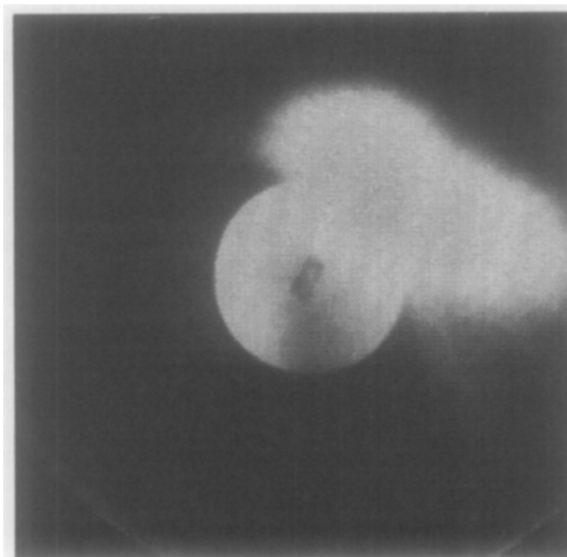


FIG. 1a. The 1st, 9th, and 17th frames after impact from the top view film records of an alumina target. The elapsed times are ~0.1 msec, ~1.4 msec, and ~2.7 msec, respectively. The projectile was shot from the right into the upper-right surface of the target.

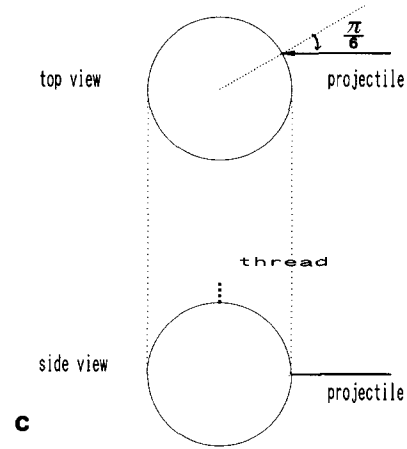
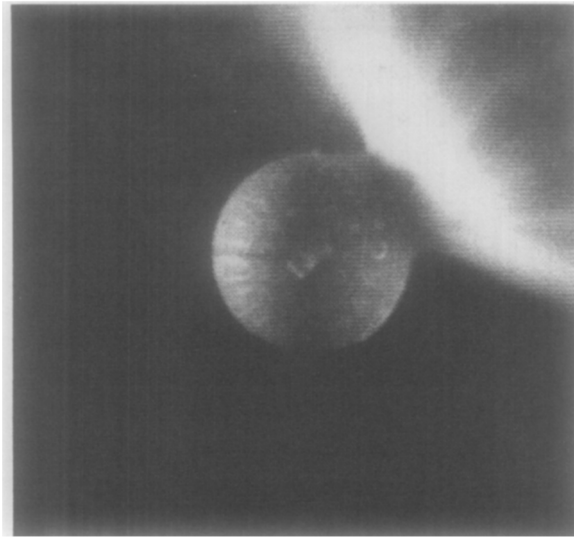


FIG. 1c. Experiment configuration.

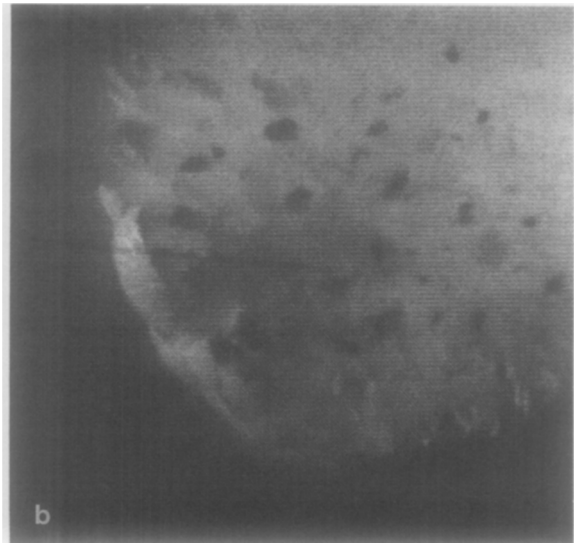
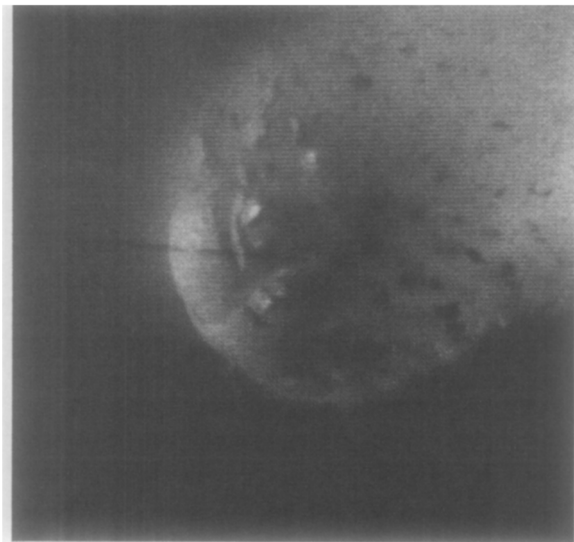


FIG. 1b. The same as Fig. 1a, but for a basalt target.

core). Their masses are shown in Table I. Fragments could be divided into three groups: the core, fine fragments near the impact site, and larger fragments (envelope) other than the core. The envelope consists of only a few layers: surface fragments (whose total mass fraction to the original target mass was more than 0.57 for alumina (a) and 0.35 for basalt (b), respectively) and intermediate fragments.

The basalt core was several times heavier than that expected for a normal incident (90° to the surface) impact (Fujiwara and Tsukamoto 1980). Data on alumina destruction experiments is sparse. The other three normal shots performed under the conditions similar to those shown in Table I resulted in almost the same core mass. However, it is difficult to discuss core-mass dependence on incident angle because of a lack of data.

For fragments which could not be identified with recovered fragments, a mass estimated from their image size was assigned, using the following mass-size relation and its extrapolation to smaller size ranges. The fragment size s , measured on the films, and the corresponding recovered mass m are plotted in Figs. 2a and 2b. The following relation holds between mass and size:

$$m = L(s) \cdot \rho \cdot s^3, \quad (1)$$

where, ρ denotes density, and $L(s)$ is a shape factor, which is determined from the linear fits as

$$L_A(s) \cdot \rho_A = (1.06 + 0.22/-0.19) \cdot s^{-0.11 \pm 0.16} \quad (1a)$$

for alumina (a), or

$$L_B(s) \cdot \rho_B = (0.82 + 0.34/-0.24) \cdot s^{0.42 \pm 0.35} \quad (1b)$$

for basalt (b). All units are in cgs. At least five fragments for the alumina shot and six fragments in the basalt shot

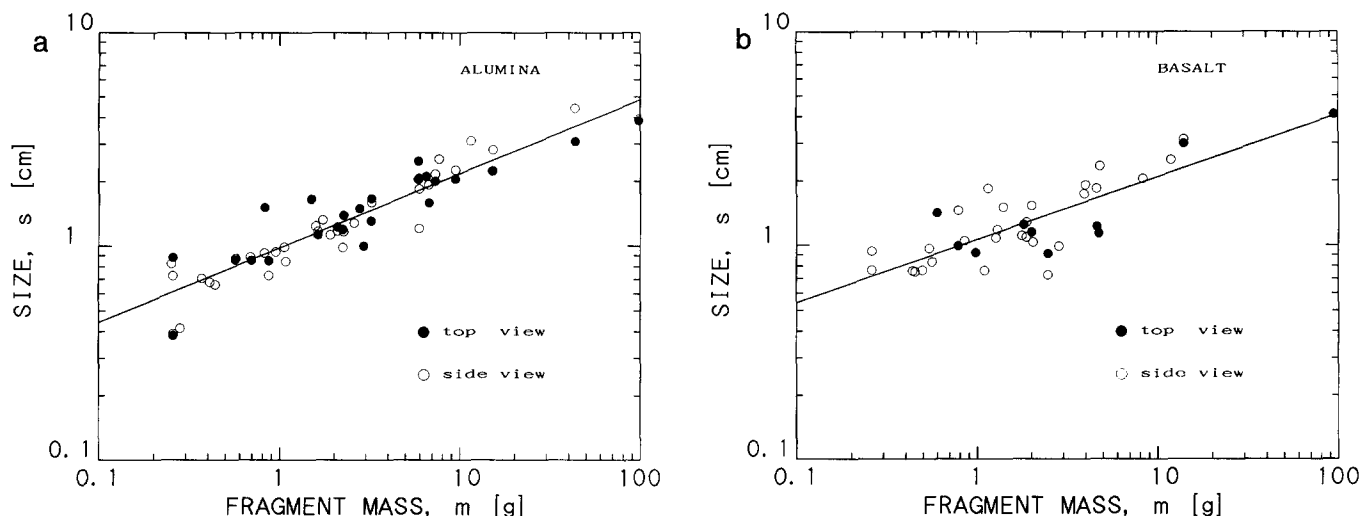


Fig. 2. (a) The 2-D image size versus measured fragment mass for the alumina target. The line represents the least square fit to the data expressed as Eq. (1). (b) The same as (a), but for fragments from the basalt target.

were secondarily fractured. They appeared as single fragments on the film, but were found to consist of a few pieces of the recovered fragments. The sum of the constituent masses was adopted for these fragments.

Figures 3a and 3b show the cumulative mass distribution obtained from the top-view pictures using the mass-size relation (Eq. (1)) and the recovered fragment mass distribution, for the alumina (a) and basalt (b) shots, respectively. The five alumina fragments and the six basalt ones mentioned above were treated as single fragments in the plots. Most of the larger fragments were tracked on the films, but the smaller ones were likely to be missed. For alumina, both mass distributions

are similar with a node (change in slope) occurring at a mass between $10^{-2.5} \cdot M_t$ and $10^{-3.5} \cdot M_t$, where M_t denotes target mass. For basalt, the nodes between $10^{-3} \cdot M_t$ and $10^{-4} \cdot M_t$ are fainter than those found in the alumina. The number of the small fragments measured from the films was fewer for the basalt than for the alumina because the basalt fragments were harder to observe due to low contrast of the image. Table I shows the total recovered mass $M_{\text{rec}} (\geq 0 \text{ g})$, and the recovery rate was more than 99%. Among them the masses of the fragments heavier than 5 mg were measured and their total mass is shown as $M_{\text{rec}} (\geq 5 \text{ mg})$ in the table.

To extrapolate the measured fragment mass distribution

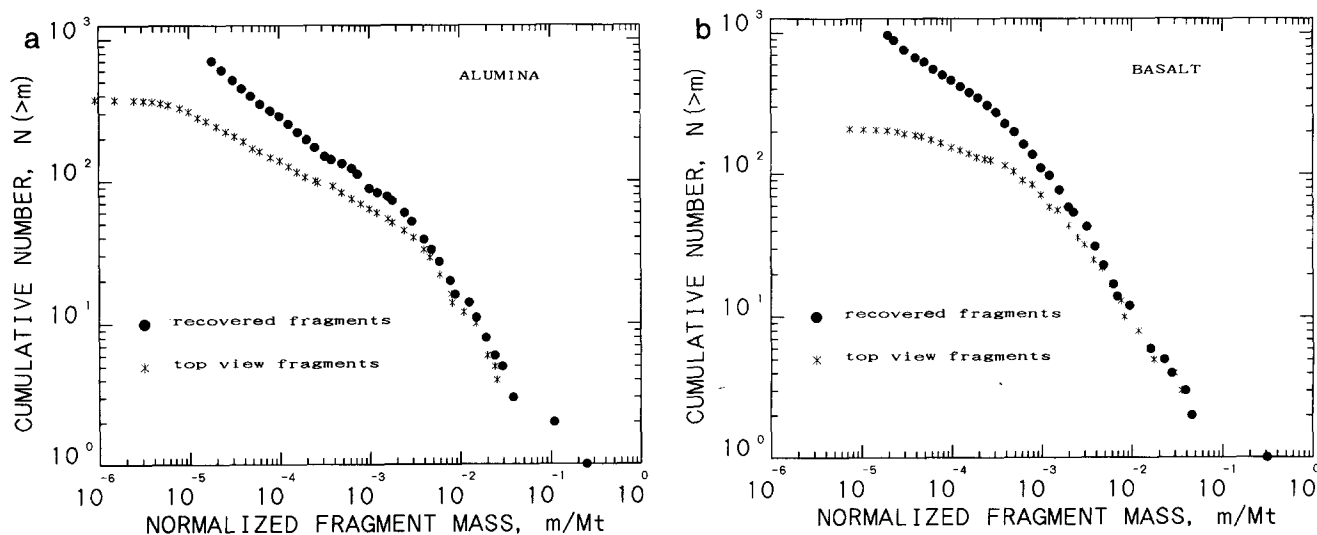


Fig. 3. (a) Cumulative number of fragments versus fragment mass for the alumina target. The masses of the top view fragments were estimated from the 2-D image size using Eq. (1). (b) The same as (a), but for fragments from the basalt targets.

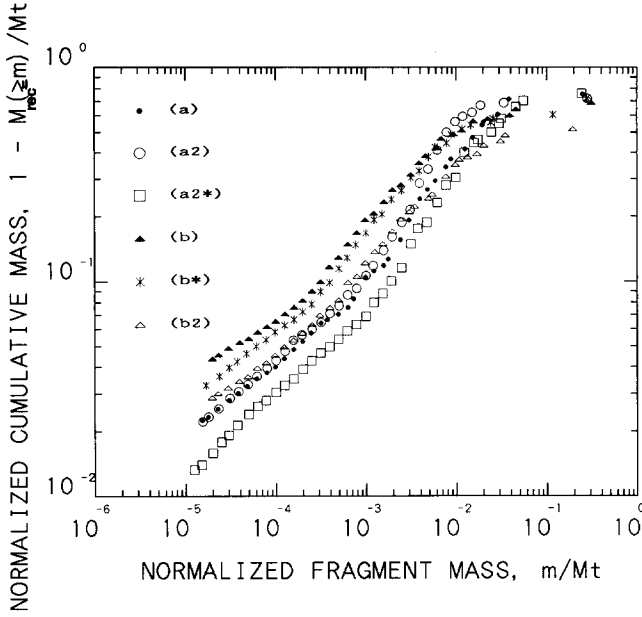


FIG. 4. Cumulative mass distribution of fragments of alumina (a-series) and basalt targets (b-series). Impact conditions are given in Table I. (b) and (b*) conducted under similar impact conditions resulted in similar distributions. (b2), obtained by using soft walls, is depleted in smaller fragments and different from both (b) and (b*). While none of the three experiment conditions of (a), (a2), and (a2*) precisely coincides to the others, the mass distribution for a hypothetical impact with the same impact condition with (a) using soft materials would be between (a2) and (a2*), i.e., a milder secondary fragmentation is suggested for alumina than basalt.

to a smaller mass range ($m < 5$ mg), the following procedure was used.

M_t can be written in terms of incremental fragment number per unit mass interval $n(m)$, the cumulative mass of recovered fragments heavier than m , $M_{\text{rec}}(\geq m)$, and the cumulative mass of the unrecovered fragments heavier than m , $M_{\text{lost}}(\geq m)$, as

$$M_t = \int_{m_0}^m n(m) \cdot m \cdot dm + M_{\text{rec}}(\geq m) + M_{\text{lost}}(\geq m), \quad (2)$$

where m_0 is the minimum fragment mass. Figure 4 shows

$$f\left(\frac{m}{M_t}\right) \equiv \frac{M_t - M_{\text{rec}}(\geq m)}{M_t}, \quad \text{for } m \geq 5 \text{ mg}, \quad (3)$$

for all six experiments. The data on unrevised recovered fragments were plotted in this figure; that is, the constituent fragments of alumina (five) and basalt (six) "single" fragments were separately adopted. Because most of the unrecovered fragments are expected to be smaller than 5

mg, we approximate $M_{\text{lost}}(\geq m) \sim 0$ for $m \geq 5$ mg. Therefore, $f(m/M_t)$ can be rewritten, using Eq. (2), as

$$f\left(\frac{m}{M_t}\right) = \frac{1}{M_t} \int_{m_0}^m n(m) \cdot m \cdot dm, \quad \text{for } m \geq 5 \text{ mg}, \quad (4)$$

The curve from Eq. (3) (or (4)) is almost straight in the mass range around $m \sim 10^{-4} \cdot M_t$. We approximate the curve by three power-law equations as discussed in the following paragraph;

$$f\left(\frac{m}{M_t}\right) = C_i \left(\frac{m}{M_t}\right)^{\delta_i}, \quad m_i < m \leq m_{i+1} \quad (i = 1, 2, 3, m_1 \geq 5 \text{ mg}, m_4 = M_t). \quad (5)$$

From Eqs. (4) and (5),

$$\frac{1}{M_t} \int_{m_0}^m n(m) \cdot m \cdot dm = C_1 \left(\frac{m}{M_t}\right)^{\delta_1}, \quad m_1 < m \leq m_2. \quad (6)$$

Extrapolating Eq. (6) to a lower mass range ($m_0 < m \leq 5$ mg), we get

$$n(m) = \frac{1}{m} \cdot \frac{d}{dm} \cdot \left(M_t \cdot C_1 \cdot \left(\frac{m}{M_t}\right)^{\delta_1} \right) \equiv n_0 \cdot m^{-\gamma}, \quad \gamma = -\delta_1 + 2 \quad (m_0 < m \leq m_2). \quad (7)$$

Table II shows n_0 and γ . Note that γ is sensitive to the interval of the experimental curve where we fit a power-law equation. Several authors report one or two inflection points in the mass distribution of the recovered fragments (Fujiwara *et al.* 1977, Di Martino *et al.* 1990, Davis and Ryan 1990), but their numbers are not in agreement. In the present study we adopt the power-law mass distribution of three segments (Takagi *et al.* 1984) because it can set a suitable interval for the straight line around $m \sim 10^{-4} \cdot M_t$ of the present data. The resultant γ is about $\frac{5}{3}$, which coincides with the results obtained by Takagi *et al.* (1984) for their "regime III." It is also similar to the size distribu-

TABLE II
Results of the Least-Squares Fits of the Experimental Mass Distribution with Eq. (7)

Target type	n_0	γ	m_1	m_2	m_0 (g)
a	15.3 ± 1.0	1.659 ± 0.012	$10^{-4.8} \cdot M_t$	$10^{-3.3} \cdot M_t$	7×10^{-5}
a2	12.66 ± 0.51	1.6306 ± 0.0067	$10^{-4.8} \cdot M_t$	$10^{-3.0} \cdot M_t$	—
a2*	8.57 ± 0.41	1.6259 ± 0.0078	$10^{-4.9} \cdot M_t$	$10^{-2.9} \cdot M_t$	—
b	29.4 ± 1.8	1.708 ± 0.022	$10^{-4.7} \cdot M_t$	$10^{-3.5} \cdot M_t$	3×10^{-4}
b*	20.2 ± 1.2	1.677 ± 0.012	$10^{-4.7} \cdot M_t$	$10^{-3.6} \cdot M_t$	2×10^{-5}
b2	14.3 ± 1.2	1.658 ± 0.015	$10^{-4.7} \cdot M_t$	$10^{-3.3} \cdot M_t$	—

tion obtained by Asada (1985) for smaller ($1 \mu\text{m} \sim 100 \mu\text{m}$) sized basalt fragments created by a little more violent collision ($E/M_t \sim 9.33 \times 10^7 \text{ ergs/g}$; E , projectile kinetic energy) and captured by styrofoam board.

Substituting Eq. (7) into Eq. (4) and $m = 5 \text{ mg}$, we might get m_0 . However, the calculated m_0 is greatly affected by the recovery rate as well as n_0 and γ , i.e., the mass distribution we adopt. m_0 is tabulated in Table II in case a finite m_0 is determined. We couldn't get m_0 for (a2), (a2*), and (b2), where γ was determined to be smaller compared to those of the others (and the secondary fragmentation was assumed to be milder as discussed in the following). More realistic γ for fine fragments in (a2), (a2*), and (b2) could be larger, i.e., comparable to $\frac{2}{3}$.

From the results described above, we suggest that the power-law mass distribution of $n(m) \propto m^{-3/5}$ may be the general rule for comminuted fine fragments.

The increase in the number of smaller fragments in (b) and (b*) (Fig. 4) is probably due to secondary fragmentation induced as the ejecta strike the walls of the experimental box. Hartmann (1978) showed that a centimeter-sized basalt block with kinetic energy more than several 10^6 ergs/g or a velocity more than a few tens of meters per second broke when it was dropped on a rocky plane surface. In the present experiment, not a few fragments have higher velocity than a few tens of meters per second as shown later. Therefore, the secondary fragmentation is highly probable. For the case of alumina (a), a minor secondary fragmentation effect was detected, probably because of the larger strength of the material, though the experimental conditions were not tuned to each other well enough to compare the outcomes. We suppose the (b2) mass distribution to be more realistic than the (b) one, and refer to it when mass distribution is required for a calculation of kinetic energy of fragments in Section 5.

Velocity of the Fragments (Mass-Velocity Distribution)

Initial positions and the velocities were determined from the observed trajectories of the fragments. Although the framing rate was too low to resolve the instant of the impact, the first frame on which phenomena are recorded is estimated to be $67 \mu\text{s}$ from the initial contact between the projectile and the target. Two-dimensional (2-D) velocities for the fragments are plotted against mass in Figs. 5a and 5b where the dashed line refers to the three-dimensional velocity shown later. Note that the smaller and slower fragments from the inner part of the target are depleted because it is difficult to recognize them as clear images on the film. Fragments flying away faster than about 100 m/sec could not be tracked.

For both (a) and (b), some of the fragments seen in the top-view film could be identified as the same fragments seen in the side-view film. The corresponding (3-D) veloci-

ties for these fragments are shown in Figs. 6a and 6b with 3σ error bars arisen from the mass and 3-D velocity estimations as stated in Section 3. The velocity was found to decrease gradually with increasing mass. A linear fit to the data gives a power law relation between fragment 3-D velocity $V(m)$ (m/sec) and mass (excluding the core, because its 3-D velocity is too small to be fitted by the same power-law relation) such that

$$V(m) = V_0 \cdot (m/M_t)^{-\beta}, \quad (8)$$

where

$$\beta_A = 0.174 \pm 0.018, V_{0A} = 4.4 + 1.5/-1.1 \text{ (m/sec)}, \quad (8a)$$

for alumina (a), and

$$\beta_B = 0.155 \pm 0.050, V_{0B} = 6.4 + 8.5/-3.6 \text{ (m/sec)} \quad (8b)$$

for basalt (b), i.e.,

$$\beta_A \sim \beta_B \sim \frac{1}{6}. \quad (8')$$

Most of the data points considerably scatter around the dashed lines. The error bars only represent the observational errors. Therefore, the deviation larger than 3σ illustrates the amount of the intrinsic scatter in the mass-velocity distribution.

Because there are more or less errors in the determination of both 3-D velocity and mass for individual fragments, a weighted least squares fit was used to obtain β and V_0 . The problem was to evaluate the statistical weight of mass. The fragment mass was determined by the two different methods. Measured mass after recovery was assigned to some of the fragments ("mass known" fragments). The ambiguity of the measured mass is about 1 mg or a little larger. Since some of the fragments were ground or chipped by the secondary fragmentation, a little ambiguity in the estimation of mass is present. The mass of the fragments which were not weighted ("mass unknown" fragments) was estimated from the mass-size relation (Eq. (1)). The weighted least squares fit is governed by the relative magnitude of the statistical weights assumed for the mass known fragments compared to those for the mass unknown fragments. We assumed the ambiguity of $\log(m/M_t)$, σ_m , as,

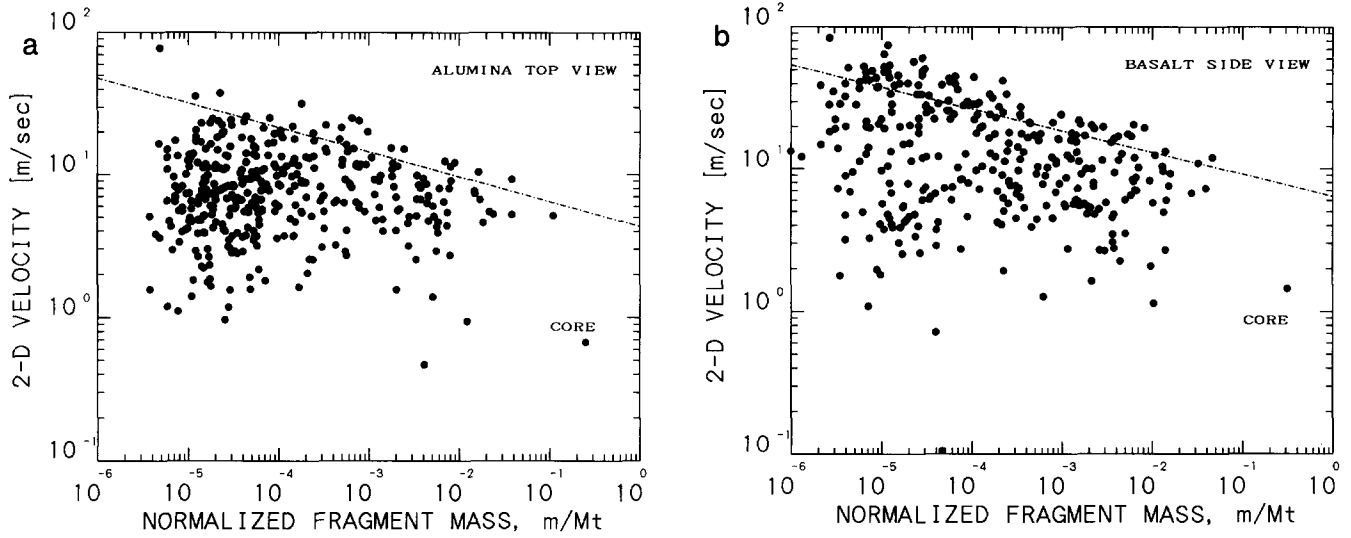


Fig. 5. (a) Mass-velocity (2-D) distribution of fragments from alumina target. The dashed line represents the 3-D velocity determined from Eq. (8). (b) The same as (a), but for fragments from the basalt target.

$$\sigma_m \begin{cases} = \text{a standard error arisen from using the mass-size relation (for mass unknown fragments),} \\ = \Delta m / M_t, \Delta m = 5 \text{ mg (for mass known fragments).} \end{cases}$$

Even if we change Δm from 1 mg to 10 mg, the conclusion shown in Eq. (8') is not changed. If we estimate fragment mass by the mass-size relation for all fragments, that is, treat all of the fragments as mass unknown, we obtain

$$\beta_A = 0.162(\pm 0.019) \quad \text{and} \quad \beta_B = 0.170(\pm 0.033), \quad (8'')$$

which coincide well with Eqs. (8a), (8b), or (8').

In Figs. 5a and 5b, the highest velocity in any given mass range is considered to represent the 3-D velocity. The upper boundary of the velocity distribution in Figs. 5a and 5b shows good agreement with the above relation of Eq. (8').

If the two or three different slopes in the size distribu-

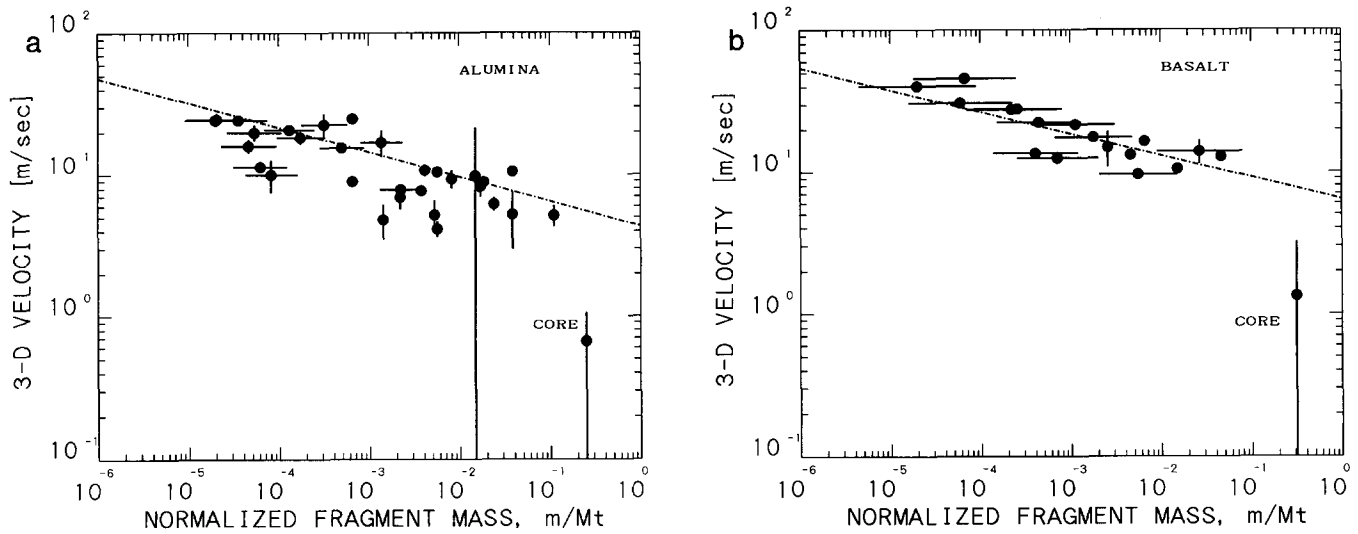


Fig. 6. (a) The mass-velocity (3-D) distribution of fragments for the alumina target, and the 3σ error bars associated with each evaluation. The dashed line represents the least squares fit to the data as expressed by Eq. (8). (b) The same as (a), but for fragments from the basalt target.

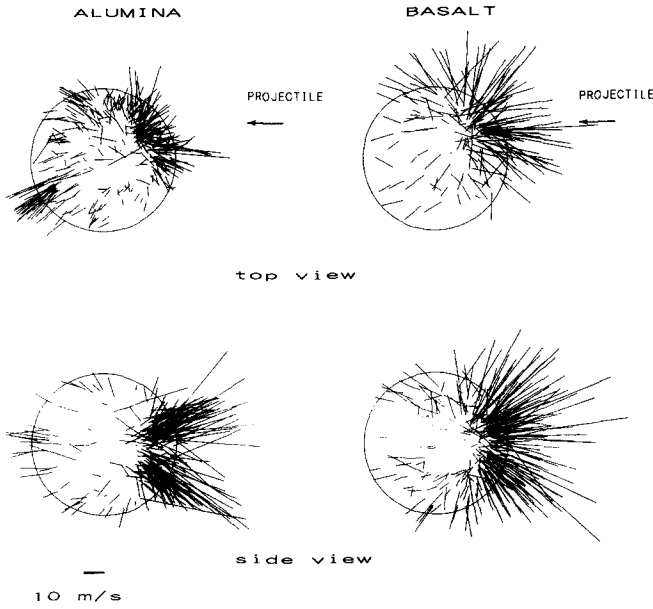


FIG. 7. Two-dimensional velocity vectors. The arrowheads are omitted.

tion are related with any fracturing process, some evidence in the mass-velocity distribution may appear, but no significant feature is found.

Position-Velocity Relation

Figure 7 shows the 2-D velocity vectors drawn from their initial positions. The basalt target showed no velocity enhancement at the antipode. The antipodal velocity (~ 10 m/sec) was about the same as in previous reports (Fujiwara and Tsukamoto 1980, Takagi and Mizutani 1984, Davis and Ryan 1990). For the alumina target, as reported for glass targets (Gault and Wedekind 1969), the antipodal velocity, typically, 20 m/sec, was larger than that at the nearby places. The semiempirical model (Paolicchi *et al.* 1989) does not reproduce this features.

In Figs. 9a and 9b, the magnitude of the 2-D velocity vector and the velocity vector angle ϕ (in the top view pictures) are plotted against the initial position angle Θ , where Θ is defined as the angle between the surface normal vector at the impact point and the one at the initial position of the fragment in the 2-D image, and ϕ is the angle between the velocity vector of the fragment and radial direction at its initial position ($-\pi < \Theta, \phi \leq \pi$) (see Fig. 8). The 2-D distance between the initial position of a fragment and the target center is represented by r^* . Fragments with smaller r^* are from the inner part of the target or from the target surface toward us. Other fragments with larger r^* are from near the target surface and we observe almost the 3-D velocity of these fragments. Fragments with larger r^* ($r_t/2 \leq r^* \leq r_t$, where r_t denotes

the target radius, and note that the core radius was in the range of $r_t/2 \sim 2 \cdot r_t/3$) are denoted by open ellipsoids. Both axes of the ellipsoids correspond to the ambiguities associated with the determination of 2-D position and velocity. Fragments with smaller r^* ($r^* < r_t/2$) are denoted by filled circles. The magnitudes of their ambiguities are of a similar order of magnitude to those shown by the open ellipsoids. The other fragments with improper r^* ($r^* > r_t$) were omitted. All of four plots (Figs. 9a and 9b) indicate that the velocity field, even in an oblique impact, is almost axially symmetric about the surface normal at the impact point (this axis is referred as the I-axis). We could not measure the velocity of individual fast fine fragments from near the impact point ($|\Theta| \leq \sim \pi/6$; estimated from both the reconstructed target and Figs. 9a and 9b) as mentioned below. Hence the data at about $\Theta = 0$ are lacking in those of higher velocity. This is why the fragments close to the impact point seem in the mean slower than or comparable to the others. The solid curves in Figs. 9a and 9b are fits by polynomial to the data denoted by open ellipsoids. Fittings were made in the angle range of $\pi/6 \leq |\Theta|$. The ϕ -plots of Figs. 9a and 9b are compared with a "radiant point" model. Paolicchi *et al.* (1989) express the velocity field at each point P in the target by

$$V(r) = V_R + V_B = \omega_0 \times OP + K(r) \cdot QP,$$

where O denotes the target center and $r = OP$, ω_0 is the initial rotation rate vector of the target, and Q is the radiant point from which all the velocity vectors radiate. The first term is the rotational part, and includes the impact-transferred angular momentum. In the present study we neglect the first term. The direction of the velocity vector is parameterized only by the distance of the "radiant point" from the target center, $d = |OQ|$. The fitting is best for $d = 1.4$ cm for the alumina data and $d = 1.9$ cm

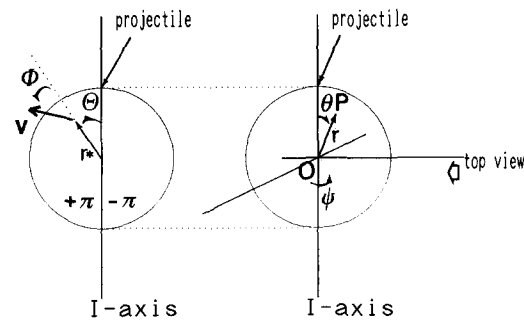


FIG. 8. The coordinate system. On the right is the three-dimensional perspective, and on the left is the coordinate system projected on a plane which includes the I-axis and is perpendicular to the (top view) line of sight (the same as the upper figure of Fig. 1c).

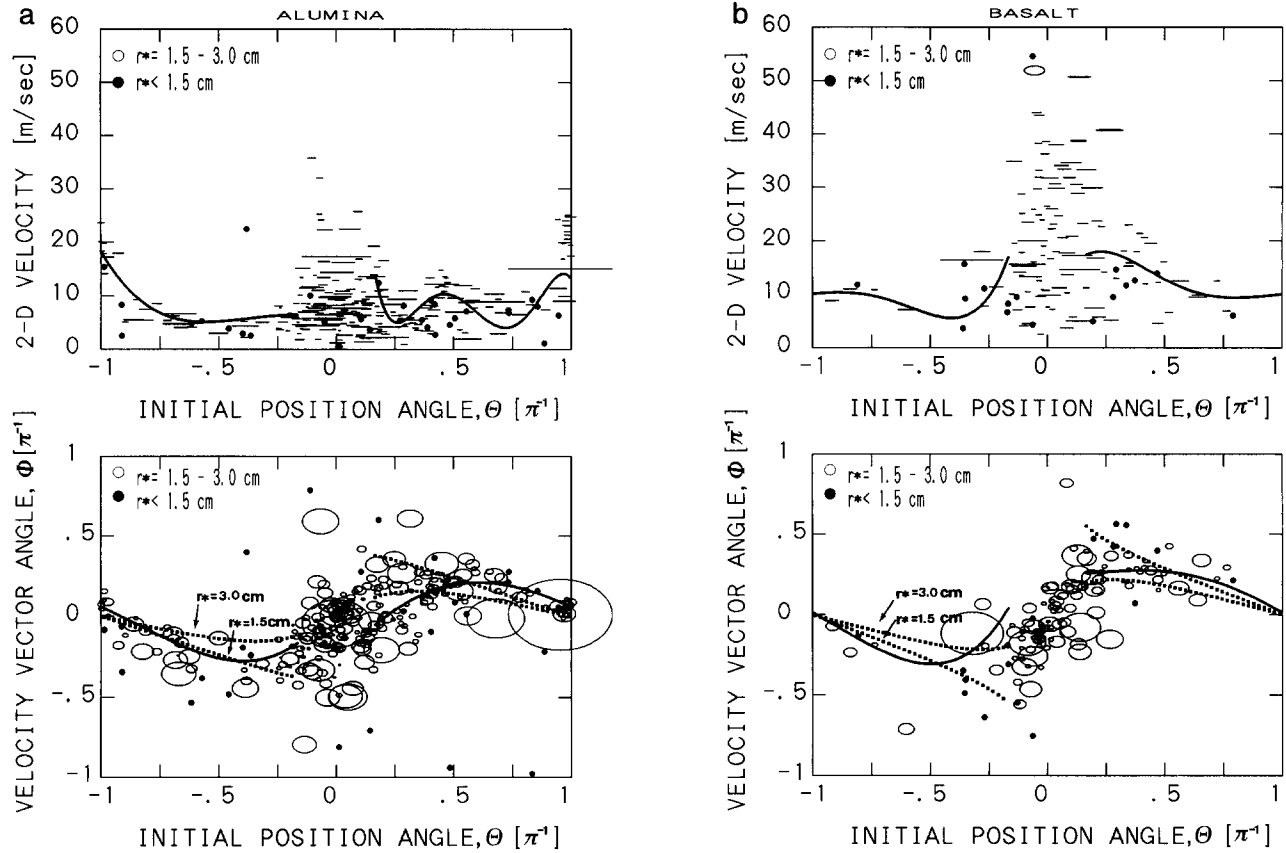


Fig. 9. (a) Position-velocity (2-D) distribution of the fragments from the alumina target. The upper plot shows the magnitude of velocity vector versus initial position of fragments. The lower plot shows the direction of the velocity vector (see Fig. 8). r^* denotes the 2-D distance between the initial position of a fragment and the target center. Fragments from the inner part of the target or from the target surface toward us are represented by filled circles, and other fragments from the outer part of the target are denoted by open ellipsoids which correspond to the standard deviation (1σ) associated with the evaluation. The solid curves are the least-squares fits to the data by polynomials. The two dotted curves in the lower plot represent a "radiant point" model for $d = 1.4$ cm, where d denotes the distance between the target center and the radiant point. (b) The same as (a), but for the basalt target and $d = 1.9$ cm.

for the basalt data. The dotted curves represent sample curves of the velocity field for $r^* = r_t/2$ and r_t with $d = 1.4$ cm and 1.9 cm, respectively. Although we neglected the term of rotation, the curves are not so deviated from the experimental data, which indicates that the impact-transferred angular momentum into these fragments is minor.

In the first frame just after the impact, a cone-like ejecta cloud of very fine and fast fragments from the impact site was observed. It is impossible to distinguish individual fragments in the ejecta cloud, but the lower limit of their velocities was estimated as at least $200 \sim 300$ m/sec, and their direction was about 60° or less from the surface normal of the impact point. This corresponds to the results obtained by Asada (1985) for fragments smaller than about $100 \mu\text{m}$.

Cumulative Velocity Distribution

It is convenient to express the present data in the form of a cumulative velocity distribution, $M(>V)$, cumulative

mass of fragments with velocity higher than V , as reported by previous authors (Gault and Heitowit 1963, Davis and Ryan 1990). However, it must be emphasized that we didn't measure the velocity of all the fragments. Hence, the plotting for $M(>V)$ is made in the following three ways.

- (1) An *upper limit* is obtained by plotting

$$\frac{M_t - \sum_{V_i \leq V} m_i}{M_t} \text{ versus } V, \quad (9)$$

where m_i and V_i are mass and 3-D velocity of individual fragments.

- (2) A *lower limit* is obtained by plotting

$$\frac{\sum_{V_i > V} m_i}{M_t} \text{ versus } V. \quad (10)$$

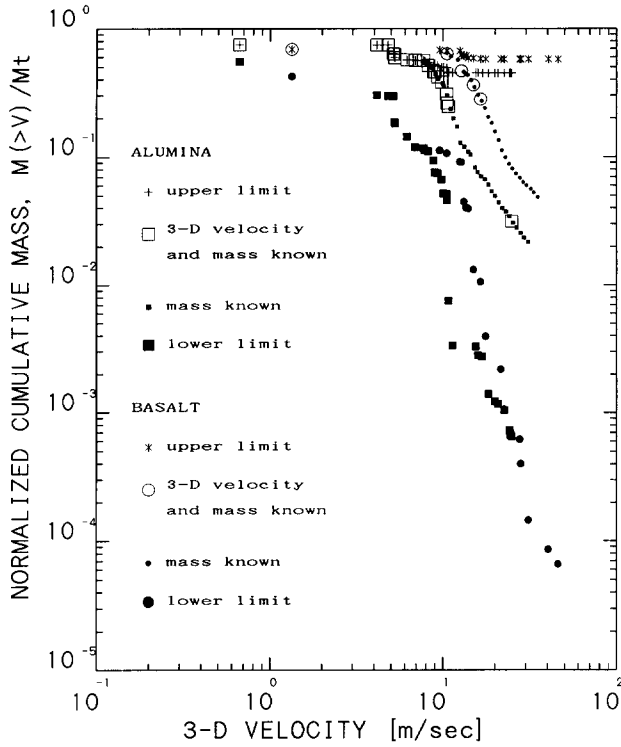


FIG. 10. Velocity-cumulative mass distribution for both the alumina and the basalt targets. The upper and the lower limits are determined from Eqs. (9) and (10). The other plots are obtained from the mass distribution of recovered fragments. 3-D velocity of fragments are estimated from fragment mass by Eq. (8) (for "mass known" fragments), while for some of the fragments both 3-D velocity and mass were measured ("3-D velocity and mass known" fragments).

(3) *An estimate using mass-velocity distribution.* Smaller filled marks in Fig. 10 show the cumulative velocity distribution plotted by using the mass-velocity distribution of Eq. (8) as well as the mass distribution of alumina and basalt. The cumulative velocity distribution, $M(>V) \propto V^{-\nu}$, is given by

$$M(>V) = \int_{m_0}^{m(V)} n(m) \cdot m \cdot dm = n_0 \cdot \left(\frac{m^{2-\gamma}}{2-\gamma} \right)_{m_0}^{m(V)} \\ \sim \frac{n_0}{2-\gamma} \cdot M_t \cdot \left(\frac{V}{V_0} \right)^{(\gamma-2)/\beta}.$$

Therefore the power index is

$$\nu = \frac{2-\gamma}{\beta} \sim 2 \quad (\gamma = \frac{5}{3}, \beta = \frac{1}{6}).$$

The estimated slope is a little more gentle than that obtained by Gault and Heitowit (1963). Note that β could be smaller because we obtained the mass-velocity distribution for fragments mostly from the surface of the target

which would have higher velocity compared with fragments from the inner part of the target. Hence ν could be slightly larger.

5. DISCUSSION

Energy Balance

From our experimental results (as expressed in Eq. (8)), the velocity of the fragments can be written as a function of their mass,

$$V \propto m^{-(1/6+f)}, \quad (11)$$

where

$$f = 0.007 \pm 0.018 \quad (11a)$$

for alumina (a) and

$$f = -0.012 \pm 0.050 \quad (11b)$$

for basalt (b). The f -values for alumina and basalt are approximately equal within errors, and are small compared to $\frac{1}{6}$. The translational kinetic energy ε_t of a fragment is a function of its mass, and using Eq. (11) can be written as:

$$\varepsilon_t \propto m^{2/3-2f}. \quad (12)$$

On the other hand, the comminution energy ε_s has the form

$$\varepsilon_s = m^{2/3} \cdot S(m) \cdot q, \quad (13)$$

where, $S(m)$ is a shape function defined such that $m^{2/3} \cdot S(m)$ is the total surface area of a fragment, and q denotes the energy per unit area necessary for creating new surfaces. To connect $S(m)$ and $L(s)$ in Eq. (1) to each other, we assumed randomly rotating ellipsoidal fragments. However, preferable geometrical parameters could not be determined to realize the mass-size relation of Eq. (1), probably because the individual fragments might not be observed from various directions or ellipsoid approximation for the shape of fragments might not be suitable.

In our experiments, fragment shape does not vary significantly with the mass. Capaccioni *et al.* (1986) noted a similar result for fragments down to 100 μm size. Hence, assuming that $S(m)$ is independent of mass, that is, the surface area is proportional to $m^{2/3}$, and neglecting the small factor $2 \cdot f$ in Eq. (12), we obtain

$$\varepsilon_t/\varepsilon_s = \text{const.} \quad (14)$$

This implies that impact energy is distributed to transla-

tional and comminution energy in a constant ratio for all fragment masses.

The ratio of translational energy E_t to comminutional energy E_s for the bulk of the fragments is estimated from Eq. (12) and Eq. (13). Again, assuming $S(m)$ is independent of the mass, and approximating the surface area by that of an equivalent mass sphere,

$$\frac{E_t}{E_s} = \frac{\int \varepsilon_t \cdot n(m) \cdot dm}{\int \varepsilon_s \cdot n(m) \cdot dm} = \frac{\int \frac{1}{2} \cdot m \cdot V(m)^2 \cdot n(m) \cdot dm}{\int m^{2/3} \cdot S(m) \cdot q \cdot n(m) \cdot dm} \sim \frac{\frac{10^4}{2} (V_0 \cdot M_t^\beta)^2}{q(\text{ergs/cm}^2) \left(\frac{36\pi}{\rho^2}\right)^{1/3}} \cdot \Lambda(m), \quad (15)$$

where

$$\Lambda(m) \equiv \frac{\int n(m) \cdot m^{2/3-2f} \cdot dm}{\int n(m) \cdot m^{2/3} \cdot dm} \sim 1.$$

For basalt, adopting $q = 6.6 \times 10^4$ ergs/cm² (the same value used by Gault and Heitowit (1963)), we get

$$\frac{E_t}{E_s} \sim 7. \quad (16a)$$

For alumina, q is uncertain, and is left as a free parameter. We obtain

$$\frac{E_t}{E_s} \sim 6 \times \frac{6.6 \times 10^4}{q}. \quad (16b)$$

Since the q for alumina is probably considerably higher than the q for basalt, the ratio E_t/E_s for alumina will likely be smaller than that for basalt. It should be noted that the ratios obtained here provide only an upper limit, because the roughness of the real surface is neglected and the velocity is overestimated.

The translational kinetic energy of the fragments can be estimated from Eq. (8) (or Eq. (11)) and the mass distribution of recovered fragments. The lower mass limit in the present mass distributions is 5 mg, and the smallest fragment image on the films corresponds to a fragment mass of about 1 mg. Therefore, we calculated energies for fragments heavier than 10 mg ($\sim 3 \times 10^{-5} \cdot M_t$), which compose more than 95% of the target mass. This method is referred to as method ①.

Another approach (method ②) was used to estimate the kinetic energies of the envelope fragments. The velocity vector \mathbf{V} is, in an average sense, a function of the ejection

coordinates (r, θ, ψ) , where θ is latitudinal angle and ψ is the azimuthal angle around the I-axis ($0 \leq \theta \leq \pi$, $-\pi < \psi \leq \pi$) (see Fig. 8). From the projected (two dimensional, top view) pictures (or Figs. 9a and 9b), we can approximately determine the velocity vector $\langle \mathbf{V}(\theta, 0) \rangle$ as well as $\langle \mathbf{V}(\theta, \pi) \rangle$ (averaged over r as shown in the following), because this vector would be within the plane which is orthogonal to the line of sight and includes the I-axis. We obtained $V(\theta)$ and $\phi(\theta)$ by polynomial fits to the data denoted by the ellipsoid marks in Figs. 9a and 9b (for fragments with $r_t/2 \leq r^* \leq r_t$ and $|\theta| \geq \pi/6$). $\langle \mathbf{V}(\theta, \psi) \rangle$ at any ψ is approximated by interpolating $V(\theta = \theta)$ and $V(\theta = -\theta)$ as

$$|\langle \mathbf{V}(\theta, \psi) \rangle| \equiv (1 - |\psi|/\pi) \cdot V(\theta = \theta) + (|\psi|/\pi) \cdot V(\theta = -\theta), \quad (17a)$$

$$\langle V_\psi(\theta, \psi) \rangle = 0, \quad (17b)$$

and

$$\begin{aligned} \cos^{-1} \frac{\langle V_r(\theta, \psi) \rangle}{|\langle \mathbf{V}(\theta, \psi) \rangle|} &\equiv \Phi(\theta, \psi) \\ &\equiv (1 - |\psi|/\pi) \cdot \phi(\theta = \theta) - (|\psi|/\pi) \cdot \phi(\theta = -\theta), \end{aligned} \quad (17c)$$

for

$$\pi/6 \leq \theta \leq \pi,$$

where $V_r(\theta, \psi)$ is the radial component of $\mathbf{V}(\theta, \psi)$. Integration was carried out inside the "shell" of inner and outer radius r_c and r_t , respectively for $\theta \geq \pi/6$, where r_c denotes the mean core radius, 1.89 cm for alumina (a) and 2.03 cm for basalt (b).

The results obtained by methods ① and ② are shown in Table III. The larger value for the result from method ① is reasonable, because the 3-D velocity was determined for the fragments almost from the surface of the target except for some fragments. The measured fragments, which represent more than 95% of the target mass, received only 1% of the impactor kinetic energy. Furthermore, the energy transferred to the core is extremely small (on the order of 0.01 percent). Most of the impact energy is expended in various energy modes of fine fragments near the impact site ($\theta \sim 0$). The smaller rate of translational kinetic energy partitioned into the alumina larger (envelope) fragments than the basalt may be attributed to the larger strength of alumina.

Momentum and Angular Momentum

From our mass and velocity data, it is possible to estimate the fractions of momentum and angular momentum about the center of the target that are partitioned into the

TABLE III
Fractions of Collisional Energy Partitioned into
Core and Larger Fragments

Target type	Fragment type	Mass fraction (%)	(Kinetic) energy fraction (%)
a	Core	24.81	0.00164
	Envelope		
	Fragments ≥ 10 mg ^a	72.64	1.06
b	Shell ^b	75.19	0.501
	Core	31.15	0.0076
	Envelope		
	Fragments ≥ 10 mg ^a	68.82 ^c	1.9 ^c
	Shell ^b	68.85	1.1

^a An estimation using 3-D velocity distribution (versus mass) determined for fragments heavier than several mg and mass distribution of recollected fragments; results from method ①.

^b An estimation using the empirical formula of velocity field (i.e., velocity distribution versus initial position); results from method ②.

^c In the evaluation of the energy fraction partitioned to the envelope fragments (≥ 10 mg), the fragment mass distribution of b2 (see text and Table I) was adopted; however, the adopted mass fraction and energy fraction of the core were those of b.

core, the larger (envelope) fragments, and the other fine fragments near the impact site.

It is considered from the approximate axial symmetry in velocity vectors described in the previous section, that most of the initial angular momentum was transferred to the fast fine fragments other than those fragments whose 2-D or 3-D velocities we measured. The momentum fractions partitioned into the larger fragments except for the cores (envelope) were estimated using the same empirical formula for the velocity fields as used in the energy estimation, for the same "shell" region of inner and outer radius r_c and r_1 , respectively for $\theta \geq \pi/6$. The remaining momentum was attributed to the fine fragments near the impact site ($0 \leq \theta < \pi/6$). The results are shown in Table IV. The interrelations between momentum vectors for the core, the larger (envelope) fragments, and the fine ejecta are illustrated in Fig. 11. The magnitudes of the momentum vectors of the core, the larger fragments, and the fine fragments, normalized by the impactor momentum, are 0.073, 1.40, 0.69 for alumina and 0.12, 1.7, 0.97 for basalt, respectively. The quantities for the basalt are about 1.5 times larger than those for the alumina. However, the lateral component of the vectors for the alumina target are larger than those for the basalt target.

The rotational frequencies of the cores about the axis of the initial angular momentum vector were obtained from the top-view images, although measurement errors were significant, as shown in Table IV. Surprisingly, cores rotated inversely to the injected angular momentum. Whether this reflects any physical process or is only a statistical fluke is not clear from the present experiments.

To calculate the moment of inertia of each core, it was approximated to have a barrel-like shape, formed by cutting the sphere with two parallel planes perpendicular to the I-axis. The angular momentum fractions partitioned into the larger fragments other than the core (envelope) were estimated in a manner similar to that discussed above. Note that these quantities (obtained by integrating the angular momentum of each volume element) include both spin and orbit contributions of the envelope fragments. The angular momentum partitioned into the fine fragments was roughly estimated by calculating the total $\mathbf{r} \times \mathbf{p}$, where \mathbf{r} is the vector from the center of the target to the ejection point, the magnitude of which is assumed to be equal to the radius of the target. The total momentum attributed to the fine fragments is substituted for \mathbf{p} . Results are shown in Table IV. The estimated angular momenta turned out to be less than the initial values for both cases, probably because the values for fine ejecta were underestimated. Namely, $\mathbf{r} \times \mathbf{p}$ for individual fine fragments increases as the magnitude of r increases. The fast fine fragments near the impact site play a significant role as carriers of angular momentum especially in the alumina case. Additional results, from impacts done at various incident angles, using other target materials, are necessary for a more detailed analysis.

6. CONCLUSIONS

The velocity of fragments produced in the impact disruption of basalt and alumina targets have a power-law dependence on fragment mass. The velocities of larger (envelope) fragments were found to be in the same range, several to tens of meters per second for both target materials. Additionally, the power-law exponent was about $-\frac{1}{8}$ for both targets. This relation held for fragments with

TABLE IV
Momentum and Angular Momentum Partitioned into Core,
Larger Fragments, and Fine Fragments

Target type	Fragment type	Momentum (g · cm/sec)		Angular momentum (g · cm ² /sec) ^c
		\parallel^a	\perp^b	
a	Initial	8.48×10^4	0	12.6×10^4
	Core	$0.20 (\pm 0.22) \times 10^4$	$-0.59 (\pm 0.19) \times 10^4$	$-1.2 (\pm 0.3) \times 10^4$
	Larger fragments	$10.92 (\pm 0.08) \times 10^4$	$-4.59 (\pm 0.04) \times 10^4$	$1.8 (\pm 0.2) \times 10^4$
	Fine fragments	-2.6×10^4	5.2×10^4	$>9.6 \times 10^4$
b	Initial	6.7×10^4	0	10×10^4
	Core	$0.65 (\pm 0.11) \times 10^4$	$-0.51 (\pm 0.50) \times 10^4$	$-0.6 (\pm 0.6) \times 10^4$
	Larger fragments	$11.08 (\pm 0.24) \times 10^4$	$-3.73 (\pm 0.19) \times 10^4$	$5.3 (\pm 0.7) \times 10^4$
	Fine fragments	-5.0×10^4	4.2×10^4	$>3.4 \times 10^4$

^a Parallel to the trajectory of the projectile. Initial momentum is defined to be plus.

^b Perpendicular to the trajectory of the projectile (see Fig. 11). The right-hand side of the trajectory (in the top view) is defined to be plus.

^c Initial angular momentum is defined to be plus.

^d Calculated value to conserve the total momentum.

^e Estimated value by assuming $\mathbf{r} \times \mathbf{p}$, where \mathbf{p} is equated to the momentum of fine fragments and \mathbf{r} is estimated to the vector from the target center to the impact point.

velocities lower than about 100 m/sec and masses heavier than several milligrams. It should be noted that the $-\frac{1}{3}$ dependence was determined primarily from prominent fragments, most of which were ejected from the surface of the targets (in the present experiments, the surface fragments occupy the major portion of the envelope fragments). Accordingly, fragments from interiors of targets have lower velocities than the $-\frac{1}{3}$ relation would imply (i.e., beneath the dashed lines in Figs. 6a and 6b). Change in incident angle of a projectile could result in different mass-velocity distribution. The present analysis and results will be placed in a series of successive studies.

The $-\frac{1}{3}$ exponent implies that the translational kinetic energy of individual fragments is proportional to the two-thirds power of fragment mass, and that the rate of (translational) kinetic energy converted into comminution energy for each fragment is constant, regardless of the fragment mass. There is a peculiar relationship between the power-law mass distribution ($n(m) \sim m^{-5/3}$) and the power law energy distribution ($\epsilon \sim m^{2/3}$) such that partitioned kinetic or comminution energy for fragments in the mass range $m_a < m < m_b$ is proportional to $\log(m_b/m_a)$. Because m_a cannot be lower than the mass of molecules, $\log(m_b/m_a)$ is finite.

The total mass of recovered fragments (for masses larger than 10 mg) represents more than 95% of the original target mass for both basalt and alumina targets. The translational kinetic energy partitioned into these fragments

was estimated to be about 1% of the initial projectile kinetic energy. The bulk of the kinetic energy, momentum, and angular momentum was brought away by fast fine ejecta originated near the impact site. For each of the cases considered, the injected angular momentum was not transmitted to the core. It is not yet clear which material properties (density, material strength, Poisson ratio, etc.) determine the transfer of angular momentum, and whether the present differences between outcomes for the two targets are statistical or physically real.

A clearer picture of the kinematics in collisional fragmentation should emerge as additional data are collected under various collisional conditions. Also, an extension of the velocity and mass range of the analysis and a faster analysis method is strongly desired.

ACKNOWLEDGMENTS

We acknowledge the detailed and thoughtful comments from Drs. K. Housen, P. Paolicchi, and E. V. Ryan. K. Ishioka is thanked for her helpful suggestions. We greatly owe Dr. T. Hirata for supplying basalt targets. One of the high-speed cameras was borrowed from Dr. Y. Takagi. We are grateful to him. This work is supported by a Grant-in-Aid for Scientific Research on Priority Area (Origin of the Solar System) of Japanese Ministry of Education, Science and Culture (No. 01611005).

REFERENCES

- ASADA, N. 1985. Fine fragments in high-velocity impact experiments. *J. Geophys. Res.* **90**, 12,445–12,453.
- CAPACCIONI, F., P. CERRONI, M. CORADINI, M. DI MARTINO, P. FARNELLA, E. FLAMINI, G. MARTELLI, P. PAOLICCHI, P. N. SMITH, A. WOODWARD, AND V. ZAPPALÀ 1986. Asteroidal catastrophic collisions simulated by hypervelocity impact experiments. *Icarus* **66**, 487–514.
- DAVIS, D. R. AND E. V. RYAN 1990. On collisional disruption: Experimental results and scaling laws. *Icarus* **83**, 156–182.
- DI MARTINO, M., G. MARTELLI, P. N. SMITH, AND A. W. WOODWARD 1990. Time evolution and dust production in catastrophic fragmentation by hypervelocity impacts. *Icarus* **83**, 126–132.
- FUJIWARA, A., G. KAMIMOTO, AND A. TSUKAMOTO 1977. Disruption of basaltic bodies by high-velocity impact. *Icarus* **31**, 277–288.
- FUJIWARA, A., AND A. TSUKAMOTO 1980. Experimental study on the velocity of fragments in collisional breakup. *Icarus* **44**, 142–153.
- FUJIWARA, A., AND A. TSUKAMOTO 1981. Rotation of fragments in catastrophic impact. *Icarus* **48**, 329–334.
- FUJIWARA, A. 1987. Energy partition into translational and rotational motion of fragments in catastrophic disruption by impact: An experiment and asteroid cases. *Icarus* **70**, 536–545.
- FUJIWARA, A., P. CERRONI, D. R. DAVIS, M. DI MARTINO, K. HOLSAPPLE, K. HOUSEN, AND E. V. RYAN 1989. In *Asteroids II* (R. P. Binzel, T. Gehrels, and M. Matthews, Eds.), pp. 240–265. Univ. of Arizona Press, Tucson.
- GAULT, D. E., AND E. D. HEITOWIT 1963. In *Proceedings of the 6th Hypervelocity Impact Symposium*, Vol. 2, pp. 419–456. Firestone Rubber Co., Cleveland, OH.
- GAULT, D. E., AND J. A. WEDEKIND 1969. The destruction of tektites by meteoroid impact. *J. Geophys. Res.* **74**, 6780–6794.

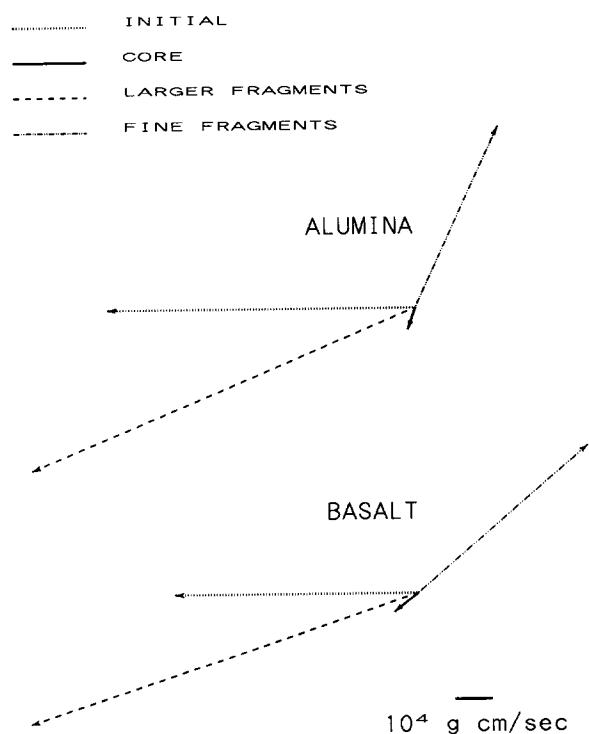


FIG. 11. The interrelation of momentum vectors.

- HARTMANN, W. K. 1978. Planet formation: Mechanism of early growth. *Icarus* **33**, 50–61.
- PAOLICCHI, P., A. CELLINO, P. FARINELLA, AND V. ZAPPALÁ 1989. A semiempirical model of catastrophic breakup processes. *Icarus* **77**, 187–212.
- TAKAGI, Y., AND H. MIZUTANI 1984. In *Proceedings of the 17th ISAS Lunar Planet Symposium*, pp. 27–28.
- TAKAGI, Y., H. MIZUTANI, AND S. KAWAKAMI 1984. Impact fragmentation experiments of basalts and pyrophyllite. *Icarus* **59**, 462–477.